

LARGE-SCALE ENERGY ATTENUATION IN TURBULENT BOUNDARY LAYER FLOW USING AN INNER-SCALED HELMHOLTZ RESONATOR

Abdelrahman H.A.S. Hassanein

Faculty of Aerospace Engineering
Delft University of Technology
2629 HS Delft, The Netherlands
a.h.hassanein@tudelft.nl

Davide Modesti

Faculty of Aerospace Engineering
Delft University of Technology
2629 HS Delft, The Netherlands

Fulvio Scarano

Faculty of Aerospace Engineering
Delft University of Technology
2629 HS Delft, The Netherlands

Woutijn J. Baars

Faculty of Aerospace Engineering
Delft University of Technology
2629 HS Delft, The Netherlands

ABSTRACT

We study how wall-bounded turbulence is affected by a single miniature Helmholtz resonator, using time-resolved planar particle image velocimetry. The wall-embedded resonator beneath the grazing flow was designed so that its natural frequency was close to the peak frequency in the wall-pressure spectrum of the turbulent boundary layer flow at a friction Reynolds number of $Re_\tau \approx 2300$. It is observed that the resonator amplifies the streamwise velocity fluctuations near resonance, while it attenuates the energy of scales at sub-resonance. The mechanism by which the resonator's local impedance condition affects the turbulent scales and how the self-resonance couples with the turbulence dynamics in the grazing flow are discussed. As such, this paper aims to address the fundamental interaction between the grazing flow and resonator physics, with a particular focus on the modification of the wall-impedance in the interaction region. Knowledge gained in this area will aid the advancement of surface designs for passive skin-friction control, using arrays of miniature resonators.

INTRODUCTION

For over four decades, a considerable research effort has been devoted to the study of turbulent skin-friction drag and control methods for mitigating this drag (Corke *et al.*, 1981). Passive methods make for appealing candidates, as they do not require energy input and are generally less complex than active systems. Helmholtz resonators (HR) show potential in controlling wall-bounded turbulence as they can be frequency tuned to the temporal scales of velocity fluctuations within wall-bounded turbulence. Panton & Miller (1975) focused on grazing TBL flow over small HRs, tuned to different portions of the wall-pressure spectrum, and exclusively considered their acoustic response. Their effect on the turbulence was partially addressed in follow-up work by Panton *et al.* (1987), Flynn *et al.* (1990) and Flynn & Panton (1990). They observed increased $\overline{u^2}^+$ and $\overline{v^2}^+$ stresses, with smaller changes in the \overline{uv}^+ stresses. No further data results were presented on energy

attenuation/amplification of specific ranges of scales in the grazing flow. Dacome *et al.* (2023) explored the interaction between a single miniature Helmholtz resonator and a grazing Turbulent Boundary Layer (TBL) flow, through varying independently its inner-scaled orifice diameter, as well as its inner-scaled resonance frequency. They revealed that behind the resonator, an amplification of the streamwise velocity fluctuations appeared at a scale close to the one of resonance. This resonance-induced amplification co-existed with a notable decrease in large-scale energy. Particularly, the changes in the spectral energy content of the flow became more pronounced when the natural frequency of the HR aligned with the peak frequency of the wall-pressure spectrum. Our current work builds upon the study of Dacome *et al.* (2023) by focusing on the resonator-flow interaction in different frequency bands, relative to the resonance scale. For this purpose, experiments are conducted using time-resolved particle image velocimetry (TR-PIV), yielding spatio-temporal data to assess the spectral variations of turbulence energy behind the resonator.

Helmholtz resonators are acoustic devices comprising an orifice and a cavity. The natural frequency of a cylindrical HR is dictated by four parameters (see Figure 1a): the orifice's diameter d , thickness t , the cavity's diameter D , and its length L . The orifice and cavity cross-sectional areas are denoted as $s = \pi d^2/4$ and $S = \pi D^2/4$, respectively, and $V = SL$ is the cavity volume. Using a mass-spring analogy, the resonator's natural frequency can be derived as shown by Alster (1972), simplifying the system to a second-order differential equation governing air displacement in the y -direction. The natural frequency (f_0) is expressed as:

$$f_0 = \frac{a_0}{2\pi} \sqrt{\frac{s}{V(t+t^*) + P}}$$

Here, a_0 represents the speed of sound, and the terms t^* and P are 'end corrections' accounting for mass displaced by the neck's mass on either side of the orifice (Ingard, 1953). A resonator interacts with the outside environment at the ori-

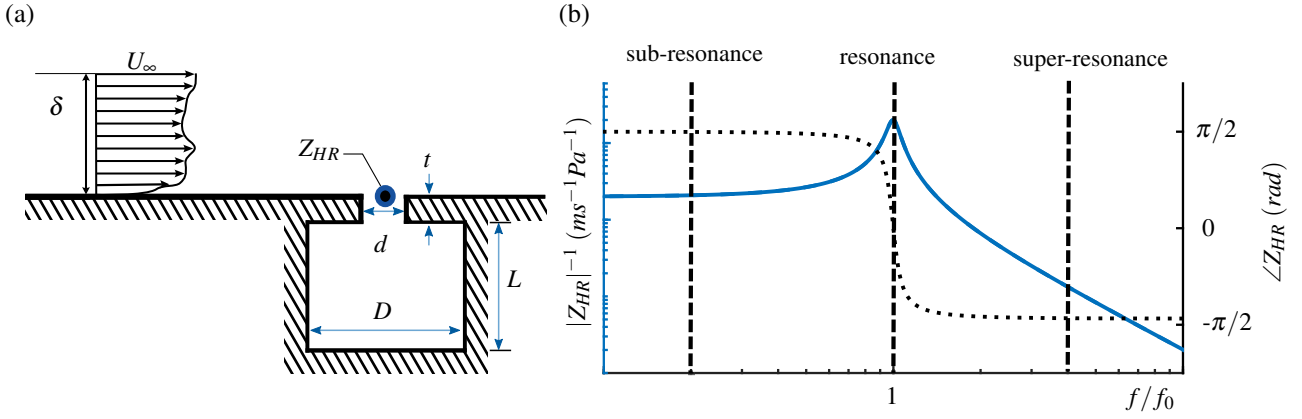


Figure 1: (a) Schematic illustration of a cylindrical Helmholtz resonator subjected to a grazing TBL flow. (b) Gain (solid) and phase (dotted) of the acoustic impedance of a single Helmholtz resonator.

face interface. Its interaction is frequency-dependent and can be expressed in terms of an acoustic impedance. It is defined as the ratio between the co-existing pressure at the orifice, p_o , and the wall-normal velocity, v_o , by way of a complex-valued kernel in the frequency domain: $Z_{HR} = p_o(f)/v_o(f)$. A typical gain and phase curve of the acoustic impedance is drawn in Figure 1b. Under acoustic excitation, the resonator will amplify a narrow band of pressure waves with frequencies close to resonance. Consequently, the oscillating mass flux through the resonator's orifice will amplify around resonance. As for the temporal phase relation, the wall-normal velocity v_o precedes the pressure at the center of the orifice p_o by a quarter of a period, for frequencies below resonance. At resonance, the wall-normal velocity and the pressure at the center of the orifice fluctuate in phase. Beyond resonance, the pressure at the orifice is ahead of the wall-normal velocity by a quarter of a cycle.

LAYOUT OF EXPERIMENTS

Flow facility and Helmholtz resonator

Experiments were conducted in a low-speed open-return wind tunnel facility (W-tunnel) comprising a zero-pressure gradient development section for a TBL flow. The cross-sectional area of the test section at the tunnel's inlet is $60 \times 60 \text{ cm}^2$. The TBL developed over a flat plate with a streamwise length of 3.75 m . The transition was initiated at the inlet of the test section on all sides using P40-grain sandpaper. Additional details of the facility are described by Baars *et al.* (2024).

In this work, $U_\tau = \sqrt{\tau_w/\rho}$ is the friction velocity, $l_v = \nu/U_\tau$ is the viscous length scale, and $Re_\tau = \delta/l_v$ is the friction Reynolds number signifying the ratio between the larger inertia-dominated scales and the smaller dissipative viscous scales. Flow conditions and TBL parameters of the nominal boundary layer flow at 3.17 m from the leading edge are summarized in Table 1.

U_∞ (m/s)	Re_τ	δ (mm)	l_v (μm)	U_τ (m/s)
15.0	2300	72.0	30.3	0.52

Table 1: Nominal TBL parameters.

bottom wall at a distance of 3.17 m from the leading edge. The considered natural frequency was tuned to match one-to-one with the peak of the wall pressure spectrum, which is known to reside at $\lambda_p^+ \approx 250$ ($f_p^+ \approx 1/25$) and to be invariant with Re_τ as elucidated by Panton *et al.* (2017). The orifice diameter was chosen as $d^+ = 60$ with two constraints in mind. First, the diameter of the orifice should be smaller than $\lambda_p^+/2$, as it will otherwise result in a spatial averaging of scales around resonance. Secondly, too small of a diameter would result in excessive viscous losses in the orifice, and weaken the ability of the resonator to affect the flow (as observed by Dacome *et al.*, 2023). The properties of the Helmholtz resonator are shown in Table 2.

d (mm)	t (mm)	D (mm)	L (mm)	f_0 (Hz)
1.8	2.4	13	22.7	723

Table 2: Properties of the Helmholtz resonator.

Flow measurement systems

Pressure measurements were conducted with the aid of GRAS46BE 1/4-in pressure-microphones, at three positions: i) within the external flow region to capture the facility noise p_f , ii) within the wall and 90 mm upstream of the resonator, using a pinhole-mounted configuration for measuring the wall-pressure signature of the incoming boundary layer, p_{tbl} , and iii) at the bottom of the resonator to capture the cavity pressure, p_c . The microphone in the free stream was equipped with a GRASRA002 nosecone to filter the turbulence-induced pressure fluctuations in the stagnation point. Time-resolved planar velocity fields were measured with high-speed PIV. Illumination was provided with a Quantronix Darwin Duo-527 Nd:YLF laser ($2 \times 25 \text{ mJ @ } 1 \text{ kHz}$). The thickness of the laser sheet was kept to 1 mm . Imaging was performed using a Photron FASTCAM SA1.1, comprising a 12-bit sensor of $1024 \times 1024 \text{ px}^2$ at 5.4 kHz , and a $20 \mu\text{m}$ pixel size. A Nikon lens with a 200 mm focal length was utilized, set to an aperture $f\#$ of 4. Additionally, a teleconverter was employed to double the optical magnification, reaching a factor of 1. The acquisition frequency was set to 14.94 kHz , and the corresponding sensor resolution was $750 \times 512 \text{ px}^2$. In total, 6 sets of 14400

A single HR was embedded in the spanwise-center of the

consecutive images were acquired uninterruptedly (thus yielding 6×14400 images per measurement case: the uncontrolled boundary layer and the resonator case). A photo of the TR-PIV setup, alongside a schematic of the resonator and field-of-view (FOV), are shown in Figure 2.

DaVis 10.2 software was used for system synchronization, image acquisition, and PIV processing. Cross-correlations of the time-resolved recordings were carried out using the sliding sum of correlations technique (Sciacchitano *et al.*, 2012) with a length of 4 frames. This approach was chosen to minimize measurement noise and enhance the robustness of correlation-peak detection. The cross-correlation employed the multi-grid window deformation method, utilizing a window size of $24 \times 6 \text{ px}^2$ ($14 l_v \times 3.6 l_v$) with a 75% overlap for the final interrogation step. The interrogation area was elongated in the streamwise direction and reduced in the wall-normal direction to enhance spatial resolution in the latter direction. Adjacent vectors were spaced at intervals of 3 px ($\Delta y^+ \approx 2$). The PIV parameters are summarised in Table 3. Finally, for each PIV dataset, fluctuating pressure measurements were conducted in a synchronized manner with a sampling frequency of 51.2 kHz . Because the Q-switch signal of the laser was also recorded, the dataset allows for conditioning PIV-based velocity fields based on events in the signals of fluctuating pressure.

Laser sheet	
Laser type	Nd:YLF
Manufacturer	Quantronix
Model	Darwin Duo-527
Maximum energy	25 mJ/pulse
Wavelength	527 nm
Thickness	1 mm
Time between pulses	$67 \mu\text{s}$
Camera	
Model	Photron FASTCAM SA1.1
Sensor resolution	$756 \times 512 \text{ px}^2$
Pixel pitch (size)	$20 \mu\text{m}$
A/D conversion	12-bit
Max. repetition rate	14940 fps
Seeding	
Type	atomized glycol-water
Nominal diameter	$1 \mu\text{m}$
Imaging conditions & analysis	
Field of view	$14 \times 9.5 \text{ mm}^2$
Image resolution	53.7 px/mm
Interrogation window	$24 \times 6 \text{ px}^2$
Processing technique	Sliding sum of correlation
Overlap	75%
Vector pitch	0.056 mm , $l_p^+ \approx 2$
Measurement rate	14.94 kHz

Table 3: PIV measurement parameters.

RESULTS

Spectral energy response of the TBL

Availability of time-resolved velocity fluctuations allow for a detailed inspection of how the resonator alters the spectral

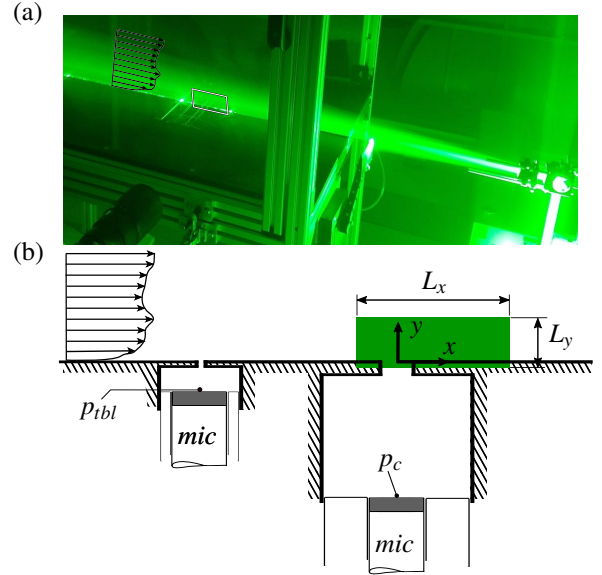


Figure 2: (a) Photograph of the TR-PIV setup. (b) An illustrative schematic showing the HR and the pinhole, along with the relative position of the TR-PIV measurement, as well as the locations of the fluctuating pressure measurements, p_{tbl} , and p_c .

energy content of the TBL flow. Figure 3a shows the absolute energy spectrogram of the uncontrolled (baseline) boundary layer flow, with alongside in Figure 3b the altered spectrogram downstream of the HR, at $x^+ = 100$. In both of these spectrograms, one can observe that the inner peak is well-captured with the TR-PIV at the location $(y^+, f^+) \approx (15; 0.01)$.

To highlight changes in the spectrograms, the percentage difference between Figure 3a and Figure 3b is plotted in Figure 3c. There is an observable narrow-band increase in the streamwise velocity fluctuations around the resonator's natural frequency. This region of increased energy is confined to a wall-normal location of approximately $y^+ = 30$ at this downstream location, and reaches up to 60% in intensification. In addition, the resonator amplifies the energy of smaller scales (i.e., higher frequencies) at super resonance, up to 20%. Furthermore, a broader band energy attenuation is observed at larger scales (i.e., lower frequencies) up to 40%, resulting in a significant depletion of energy within the spectral-inner peak as is in agreement with the observations made by Dacome *et al.* (2023).

We now proceed by examining two frequency bands, centered at $f_0^+ = 0.04$ and $f_1^+ = 0.006$. These correspond to the resonance frequency and a much lower frequency. Spatial distributions of the premultiplied streamwise fluctuation energy are shown at $f_1^+ = 0.006$ and $f_0^+ = 0.04$ for the HR case, in Figure 4a and Figure 4b, respectively. Notably, at resonance, there is a narrow plume-type region where the energy of the streamwise velocity fluctuations is increased. This region persists up to a downstream distance of at least $x^+ = 250$. To the contrary, the streamwise fluctuation energy residing at f_1^+ is attenuated in the region close to the wall, which manifests itself with a slight bending and lowering magnitude of the contour lines above and beyond the resonator orifice in Figure 4a.

Effects of the resonator on the spatio-spectral distribution of energy can be observed in Figure 4c and Figure 4d, in which the percentage difference of streamwise fluctuation energy are shown for the same two frequency bands considered earlier

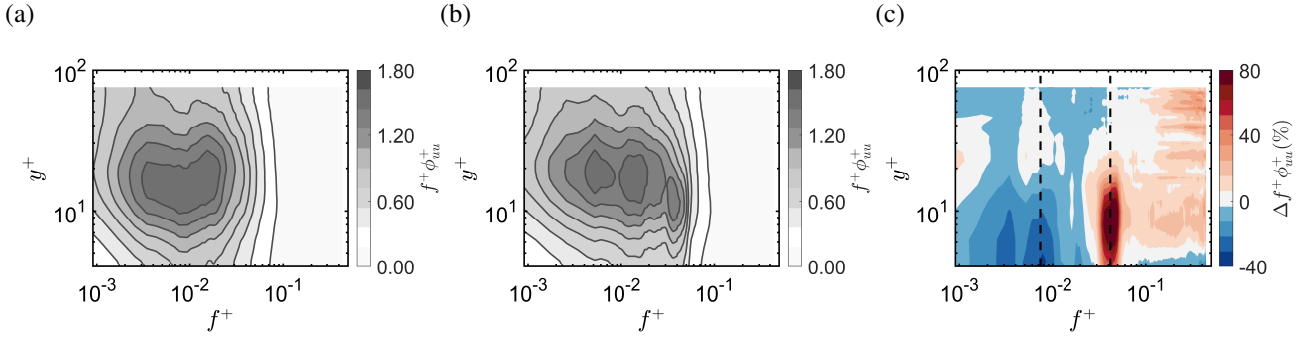


Figure 3: (a,b) Premultiplied energy spectrogram of the streamwise velocity fluctuations, $f^+ \phi_{uu}^+$ at $x^+ = 100$, for (a) the uncontrolled TBL and (b) the embedded Helmholtz resonator case. (c) Percentage difference between the premultiplied energy spectrograms presented in sub-figures (a) and (b). A positive (red) value indicates a larger energy content in the case of the embedded Helmholtz resonator; the dashed line indicates the frequencies of the contours in Figure 4.

(f_l^+ and f_0^+). Scales that get amplified by the presence of the resonator decay considerably faster in contrast to the degree by which the larger scales recover from the energy attenuation. For instance, the resonator increases the energy of the scales around the resonance frequency by more than 100% above the resonator. That energy-increase then decays and reaches a value of 5% by $x^+ = 200$. However, the attenuation in energy returns to the value of the baseline case much further downstream of the resonator as it goes from 30% at $x^+ = 75$ to 20% at $x^+ = 300$. Furthermore, the effects are confined to different regions in wall-normal direction: Resonance-related fluctuations occupy a region up to $y^+ = 20$ (Figure 4d), whilst the bulk of the effects on the attenuated scales is confined to a thin, elongated region below $y^+ \approx 10$. The latter region seems to extend far beyond the captured flow region (e.g., $x^+ \gg 300$).

Resonator-turbulence interaction

From the previous results, it is evident that the resonator influences the spectral energy content in different ways, depending on the frequency. This suggests that the frequency-dependent impedance condition at the orifice of the HR plays a role in the interaction mechanism. In this section, we postulate the interaction mechanism responsible for the observed trends. First, the assumption is made that the Helmholtz resonator locks-in with the incoming wall-pressure fluctuations of the TBL (i.e., the resonator does not change the phase of the wall pressure fluctuation). This hypothesis incorporates the observation by Jafari *et al.* (2023), in that the phase difference between the wall-normal velocity and the pressure is $\pi/2$ in a TBL for the frequencies associated with the very large-scale motion and the ones associated with the near-wall cycle. We now take a closer look at the sub-resonance, resonance, and super-resonance range of frequencies and how the wall velocity at the resonator's orifice behaves at those frequencies. Figure 5 depicts the amplitude and phase response of the wall-normal velocity (v_o) at the resonator's orifice in comparison to the pressure (p_{tbl}) and wall-normal velocity (v_{tbl}). At sub-resonance, v_o is at phase opposition to v_{tbl} , leading to the attenuation of the energy of those scales. At resonance, v_o and v_{tbl} are in phase quadrature, and the amplitude of v_o is high due to resonance, leading to energy amplification. At super-resonance, the v_o and v_{tbl} are in phase alignment, but the magnitude of v_o is negligible, leading to a considerably lower energy amplification.

In order to visualize the effect of the resonator at sub-

resonance and resonance with the aim to provide evidence for the aforementioned postulation, a contour of the conditional average of the streamwise fluctuation $\tilde{u} - \bar{u}$ on the frequencies at resonance and sub-resonance is considered. Figure 6 shows three instances during a positive streamwise fluctuation around resonance ($f_0^+ = 0.04 \pm 0.0024$) for the uncontrolled TBL and the case where the HR is embedded. Figure 7 presents data in an identical manner, but now considers a large-scale streamwise velocity fluctuation corresponding to the sub-resonance frequency, $f_l^+ = 0.006 \pm 0.0024$ ($f_l/f_0 = 0.15$). A substantial increase is observed in the conditionally-averaged streamwise velocity behind the resonator around resonance in comparison to the uncontrolled case. This increase appears to be confined in the streamwise direction as it returns to the baseline level after $x^+ = 250$. This reflects the earlier observation on the basis of the energy spectrograms. In addition, the blobs above the resonator appear to have a more round shape and a lower inclination. At sub-resonance, a notable decrease is observed in the conditionally-averaged streamwise velocity behind the resonator, for, at least, the streamwise region captured in our current measurements, $x^+ \in [0, 350]$. Further research is required to examine the total extent by which the large-scale energy is attenuated.

Following our hypothesis and discussions of supporting results, a Helmholtz resonator with grazing, broadband velocity fluctuations, will in any circumstance: 1) amplify energy at the resonance frequency, and at the frequency band beyond it, and 2) attenuate energy at frequencies below resonance. Though, when the resonator is tuned to a natural frequency that is much beyond $f^+ \approx 1/25$, the attenuation in the large-scale energy seems to be of a lower percentage at a downstream position of $x^+ = 100$ as observed by Dacome *et al.* (2023). Future research should shed further light on this issue. In addition, whether the achieved large-scale energy attenuation yields a reduction in skin-friction drag downstream is to be answered. That is, various works show a direct connection between near-wall turbulence kinetic energy production and skin friction coefficient (Deck *et al.*, 2014; Harsha & Lee, 1970).

CONCLUSIONS

This study investigates the impact of single inner-scaled Helmholtz resonators on wall-bounded turbulence using time-resolved planar particle image velocimetry (TR-PIV) at a friction Reynolds number of $Re_\tau \approx 2300$. The resonator is de-

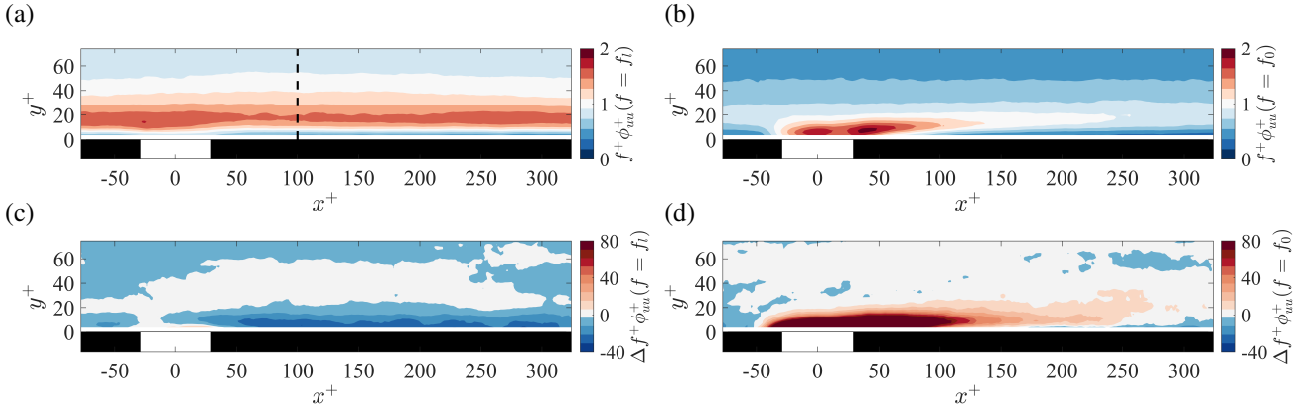


Figure 4: (a,b) Contours of the premultiplied streamwise energy for the resonator case at $f_l^+ = 0.006$ and $f_0^+ = 0.04$, respectively; the dashed line indicates the streamwise location of the spectrogram in Figure 3. (c,d) Contours of the percentage difference of the streamwise energy at f_l^+ and f_0^+ , respectively, for the case with Helmholtz resonator embedded with respect to the uncontrolled TBL.

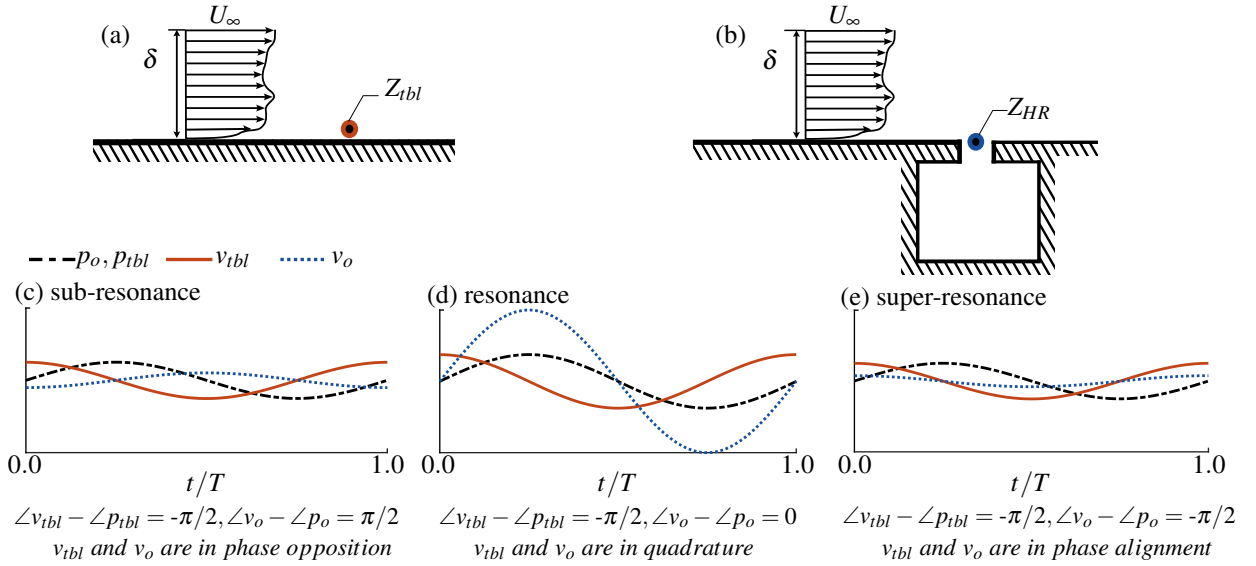


Figure 5: (a) Illustrative schematic of the impedance in a TBL. (b) Illustrative schematic of the impedance at the resonator's orifice. (c,d,e) Illustrations of one period of the temporal fluctuations of p_{tbl} , v_{tbl} , v_o for frequencies at sub-resonance, resonance, and super-resonance.

signed to match its natural frequency with the peak frequency of the wall-pressure spectrum. The resonator's frequency alignment with the peak wall pressure spectrum results in the excitation of scales near and above resonance while attenuating the energy of sub-resonant scales. This phenomenon is attributed to the local impedance at the resonator's orifice, with implications for the phase relationship between wall-normal velocity fluctuations at the resonator's orifice and wall-normal velocity fluctuations in a TBL. By disrupting the near-wall cycle and diminishing the energy of the larger structure's footprint near the wall, Helmholtz resonators placed at frequencies near the peak wall pressure spectrum demonstrate potential scalability with friction Reynolds number and applicability in the construction of control surfaces for skin-friction drag manipulation. This fundamental understanding of passive resonator-induced modifications in wall impedance offers insights into designing surfaces for effective skin friction control, potentially advancing the field toward practical applications.

REFERENCES

- Alster, M. 1972 Improved calculation of resonant frequencies of Helmholtz resonators. *J. Sound Vibr.* **24** (1), 63–85.
- Baars, W. J., Dacome, G. & Lee, M. 2024 Reynolds-number scaling of wall-pressure–velocity correlations in wall-bounded turbulence. *J. Fluid Mech.* **981**, A15.
- Corke, T.C., Guezennec, Y. & Nagib, H.M. 1981 Modification in drag of turbulent boundary layers resulting from manipulation of large-scale structures. *Tech. Rep.*. NASA.
- Dacome, G., Siebols, R. & Baars, W. J. 2023 Inner-scaled Helmholtz resonators with grazing turbulent boundary layer flow. *arXiv preprint arXiv:2308.07776*.
- Deck, S., Renard, N., Laraufie, R. & Weiss, P.-E. 2014 Large-scale contribution to mean wall shear stress in high-Reynolds-number flat-plate boundary layers up to 13650. *J. Fluid Mech.* **743**, 202–248.
- Flynn, K. P. & Panton, R. L. 1990 The interaction of Helmholtz resonators in a row when excited by a turbulent boundary layer. *J. Acoust. Soc. Am.* **87** (4), 1482–1488.

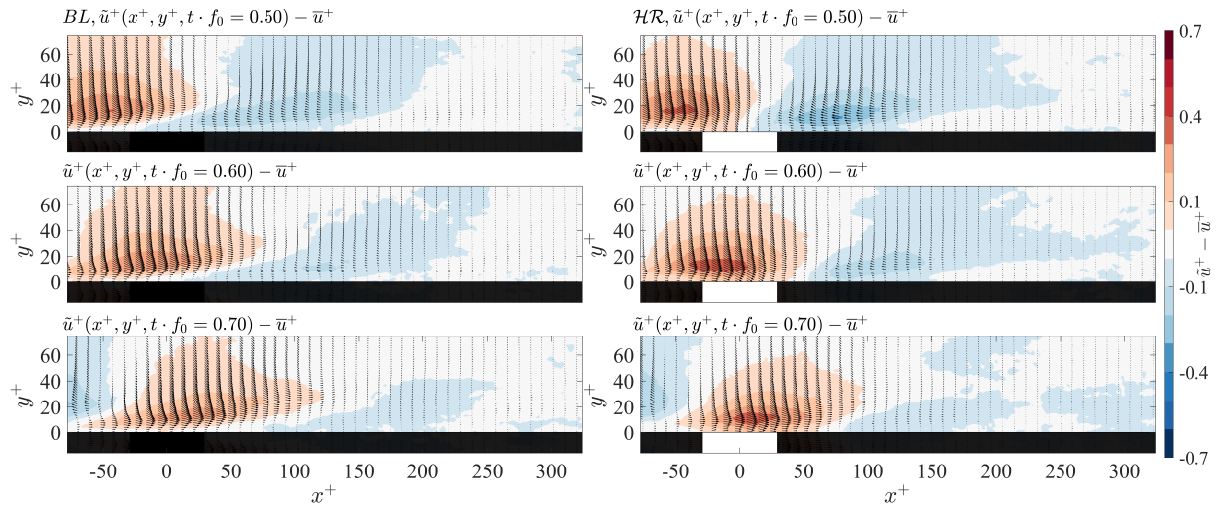


Figure 6: Three instances of the conditionally-averaged streamwise velocity fluctuation around resonance ($f_0^+ = 0.04 \pm 0.0024$) for the uncontrolled TBL on the left and the case where the Helmholtz resonator is embedded on the right.

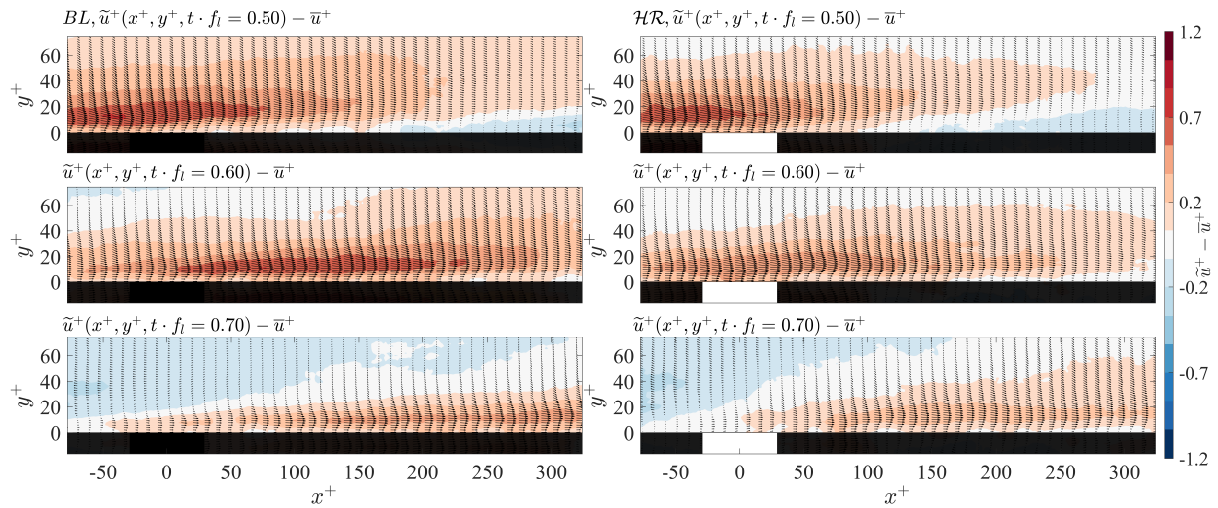


Figure 7: Three instances of the conditionally-averaged streamwise velocity fluctuation at sub-resonance ($f_l^+ = 0.006 \pm 0.0024$) for the uncontrolled TBL on the left and the case where the Helmholtz resonator is embedded on the right.

Flynn, K. P., Panton, R. L. & Bogard, D. G. 1990 Effect of Helmholtz resonators on boundary-layer turbulence. *AIAA J.* **28** (11), 1857–1858.

Harsha, P. T. & Lee, S. C. 1970 Correlation between turbulent shear stress and turbulent kinetic energy. *AIAA J.* **8** (8), 1508–1510.

Ingard, U. 1953 On the theory and design of acoustic resonators. *J. Acoust. Soc. Am.* **25** (6), 1037–1061.

Jafari, A., McKeon, B. J. & Arjomandi, M. 2023 Frequency-tuned surfaces for passive control of wall-bounded turbulent flow – a resolvent analysis study. *J. Fluid Mech.* **959**, A26.

Panton, R. L., Flynn, K. P. & Bogard, D. G. 1987 Control of turbulence through a row of Helmholtz resonators. In *AIAA Paper 1987-0436*.

Panton, R. L., Lee, M. & Moser, R. D. 2017 Correlation of pressure fluctuations in turbulent wall layers. *Phys. Rev. Fluids* **2**, 094604.

Panton, R. L. & Miller, J. M. 1975 Excitation of a Helmholtz resonator by a turbulent boundary layer. *J. Acoust. Soc. Am.*

58 (4), 800–806.

Sciacchitano, A., Scarano, F. & Wieneke, B. 2012 Multi-frame pyramid correlation for time-resolved PIV. *Exp. Fluids* **53** (4), 1087–1105.